ADVANCED FUNCTIONAL MATERIALS
www.afm-journal.de

# Efficient $Ni_2Co_4P_3$ Nanowires Catalysts Enhance Ultrahigh-Loading Lithium–Sulfur Conversion in a Microreactor-Like Battery

*Zihan Shen, Mengqiu Cao, Zili Zhang, Jun Pu, Chenglin Zhong, Jiachen Li, Haixia Ma, Fujun Li, Jia Zhu, Feng Pan, and Huigang Zhang**

**High-loading lithium–sulfur (Li–S) batteries suffer from poor electrochemical properties. Electrocatalysts can accelerate polysulfides conversion and suppress their migration to improve battery cyclability. However, catalysts for Li–S batteries usually lack a rational design. A d-band tuning strategy is reported by alloying cobalt to metal sites of $Ni_2P$ to enhance the interaction between polysulfides and catalysts. A molecular or atomic level analysis reveals that $Ni_2Co_4P_3$ is able to weaken the S—S bonds and lower the activation energy of polysulfides conversion, which is confirmed with temperature-dependent experiments. $Ni_2Co_4P_3$ nanowires are further fabricated on a porous nickel scaffold to unfold the catalytic activity by its large surface area. Using a simple ion-selective filtration shell, a microreactor-like S cathode (MLSC) is constructed to realize ultrahigh S loading (25 mg $cm^{-2}$). As such, a microreactor design integrates reaction and separation in one cell and can effectively address the polysulfide issues, the MLSC cell demonstrates excellent properties of cyclability and high capacity (1223 mAh $g^{-1}$ at 0.1 C). More importantly, the catalyst's designs and microreactor strategies provide new approaches for addressing the complicated issues of Li–S batteries.**

## 1. Introduction

Lithium–sulfur (Li–S) batteries hold great promise for next-generation rechargeable batteries because of their high specific energy (2600 W h $kg^{-1}$) and low cost of S.[1–3] However, there exist several serious challenges, which must be addressed for practical applications of Li–S batteries.[4–6] The dissolution of intermediate polysulfides ($Li_2S_x$, $4 \le x \le 8$) leads to the "shuttle effects," lowering the Coulombic efficiency (CE) and cyclability of Li–S batteries. The poor conductivities of S and discharge products ($Li_2S/Li_2S_2$) increase the charge transfer resistance and lower the intrinsically sluggish kinetics of the conversion reactions among S species. During cycling, the large volume change of S cathodes compounds these issues and shortens the service life of Li–S batteries. Li–S batteries with low S loading can show good cyclability. However, high-loading cells are usually unable to maintain reasonable cycling properties.[7,8]

Recent progress on Li–S batteries has demonstrated some successful strategies to address the above issues. Various metal sulfides,[6,9] oxides,[10,11] and nitrides[12–14] were studied to adsorb polysulfides to prevent polysulfides migration. Oxides usually show strong adsorption of polysulfides via dominant oxygen–lithium binding.[15,16] However, low conductivities render oxides less advantageous. Some metal sulfides have been found to adsorb polysulfides and also accelerate $Li_2S$ oxidation,[17] demonstrating the catalytic activity for polysulfides conversion. The catalytic effects not only enhance the kinetics of Li–S batteries but also reduce the possibility of polysulfides migration toward anodes. A conductive catalyst with adsorbing capability is desired to address the polysulfides-related issues. However, the catalyst developments for Li–S batteries reply more or less on trial and error, lacking in rational design.

Transition metal phosphides (TMPs) usually exhibit metallic conductivity in contrast to most oxides[18–20] and sulfides and receive increasing attention on efficient electrocatalysts for the oxygen evolution reactions. Qian and co-workers reported that the p-band of anions in Co-based compounds plays a key role in the catalysis of Li–S batteries because an appropriate anion

Z. Shen, M. Cao, Z. Zhang, J. Pu, C. Zhong, Prof. J. Zhu, Prof. H. Zhang
National Laboratory of Solid State Microstructures
Collaborative Innovation Center of Advanced Microstructures
College of Engineering and Applied Sciences,
and Institute of Materials Engineering
Nanjing University
Nanjing, Jiangsu 210093, China
E-mail: hgzhang@nju.edu.cn
J. Li, Prof. H. Ma
Department of Chemical Engineering
Northwest University
Xi'an, Shaanxi 710069, China
Prof. F. Li
Key Laboratory of Advanced Energy Materials Chemistry
(Ministry of Education)
Nankai University
Tianjin 300071, China
Prof. F. Pan
School of Advanced Materials
Shenzhen Graduate School
Peking University
Shenzhen 518055, China
The ORCID identification number(s) for the author(s) of this article can be found under https://doi.org/10.1002/adfm.201906661.

DOI: 10.1002/adfm.201906661

 

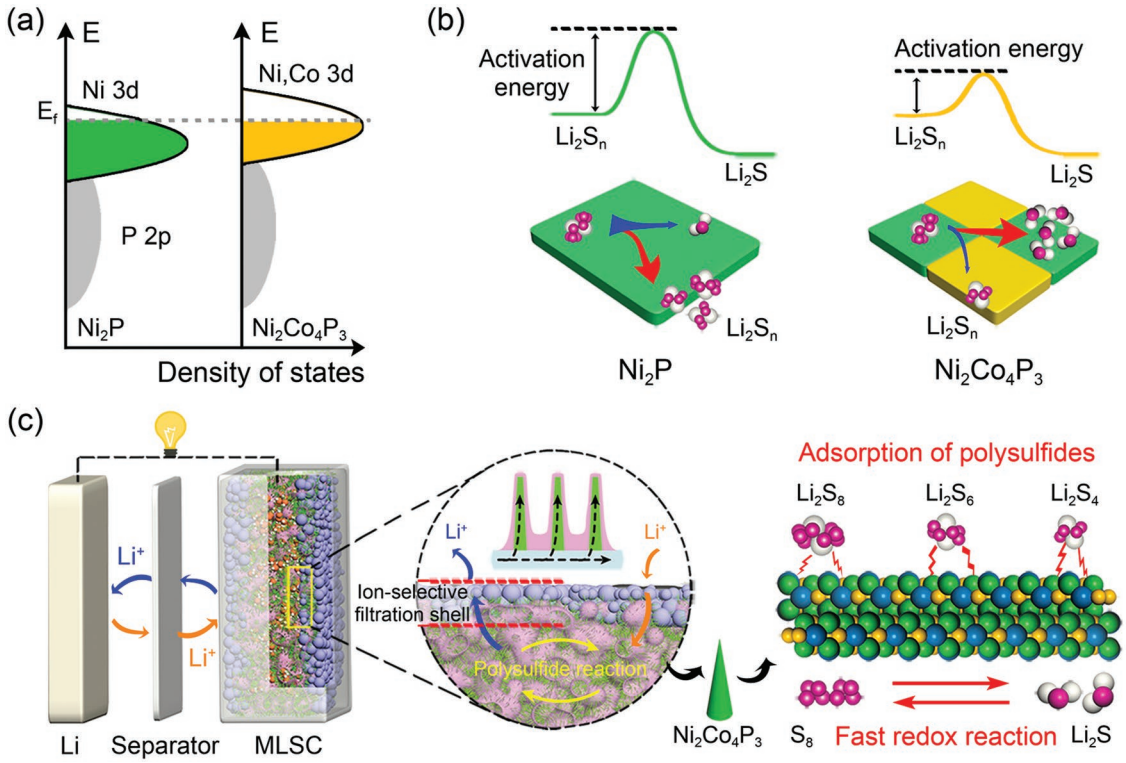


**Figure 1.** Conceptual illustration of designing catalyst and MLSC: a) density of states of Ni/Co phosphides showing the d-band shift upon Co doping, b) activation energy change of $Li_2S$ nucleation when using $Ni_2P$ and $Ni_2Co_4P_3$ as catalysts, and c) a Li–S battery using a microreactor-like S cathode that has $Ni_2Co_4P_3$ nanowires to catalyze polysulfides conversion and ion-selective filtration shell to confine polysulfides and allow Li-ion diffusion.

p-band led to rapid charge transfer at interfaces.[19] Wang and co-workers showed that Co–Fe phosphides could speed up Li–S conversion.[20] However, few studies have been reported on the molecular or atomic level picture of catalysis, which is of vital importance for a rational understanding of Li–S catalysis.

In this study, we used a metallic $Ni_2P$ as a model catalyst and substituted Ni with Co to tune and understand its catalysis activity for Li–S conversion reactions because metal phosphides have been reported as active catalysts for polysulfides conversion[18–20] and $Ni_2P$ could accept a certain degree of cation dopants and disorder within the original crystallographic framework, which provides opportunities to readily tune its d-band structure. As shown in **Figure 1**, the Co dopants in $Ni_2Co_4P_3$ raise the d-band of metal sites and further strengthen the interaction between polysulfides and catalysts, thereby lowering the activation barrier. The theoretical analysis reveals that the terminal S atoms were adsorbed to the triply bridged metal sites through a strong metal—S bond. The S—S bonds of polysulfides were weakened because of the redistributed electron population. To maximize the catalytic effect, we fabricated $Ni_2Co_4P_3$ nanowires on a highly porous nickel scaffold (PNS), yielding rapid electron and ion pathways and a high surface area for charge transfer. At last, we embedded an ion-selective filtration layer into the shallow surface of PNS to form a microreactor-like S cathode (MLSC). Fast polysulfide conversion by $Ni_2Co_4P_3$ and MLSC design significantly improve the cycling properties of Li–S batteries. By virtue of the easy scalability of microreactor strategy, we are able to realize ultrahigh S loading of 25 mg $cm^{-2}$ with a capacity of 413 mAh $g^{-1}$ (10 mAh $cm^{-2}$) until 150 cycles. The MLSC battery with 5 mg $cm^{-2}$ S can deliver a high initial capacity of 1223 mAh $g^{-1}$ and maintain an ultralow decay rate of 0.39 mAh $g^{-1}$ per cycle up to 1000 cycles. More importantly, the scalable capability and rational catalyst design make MLSC a new approach to building high-loading Li–S batteries.

## 2. Results and Discussion

### 2.1. Characterization of Li–S Battery Catalysts

$Ni_2Co_4P_3$ nanowires were synthesized via a solid-state phosphorization reaction (see the Experimental Section for details). Figure S1 in the Supporting Information presents the characterization results of the precursors $NiCo_2(CO_3)_{1.5}(OH)_3 \cdot xH_2O$ using X-ray diffraction (XRD), scanning electron microscopy (SEM), and transmission electron microscopy (TEM) technologies. They indicate that the hydrothermally synthesized precursors have nanowire morphology, which can be retained after phosphorization at 300 °C as shown in Figure S2 in the Supporting Information. The further analyses using XRD, energy-dispersive X-ray (EDX), and inductively coupled plasma-optical emission spectroscopy show that the phosphorized nanowires adopt a hexagonal $Ni_2P$ structure (Joint Committee on Powder Diffraction Standards No. 71-2336) with a 1:2 atomic ratio of Ni:Co in metal sites.

Reaction kinetics of Li–S batteries using $Ni_2P$ and $Ni_2Co_4P_3$ catalysts was studied by various electrochemical techniques as shown in **Figure 2**. It is well known that Li–S batteries usually

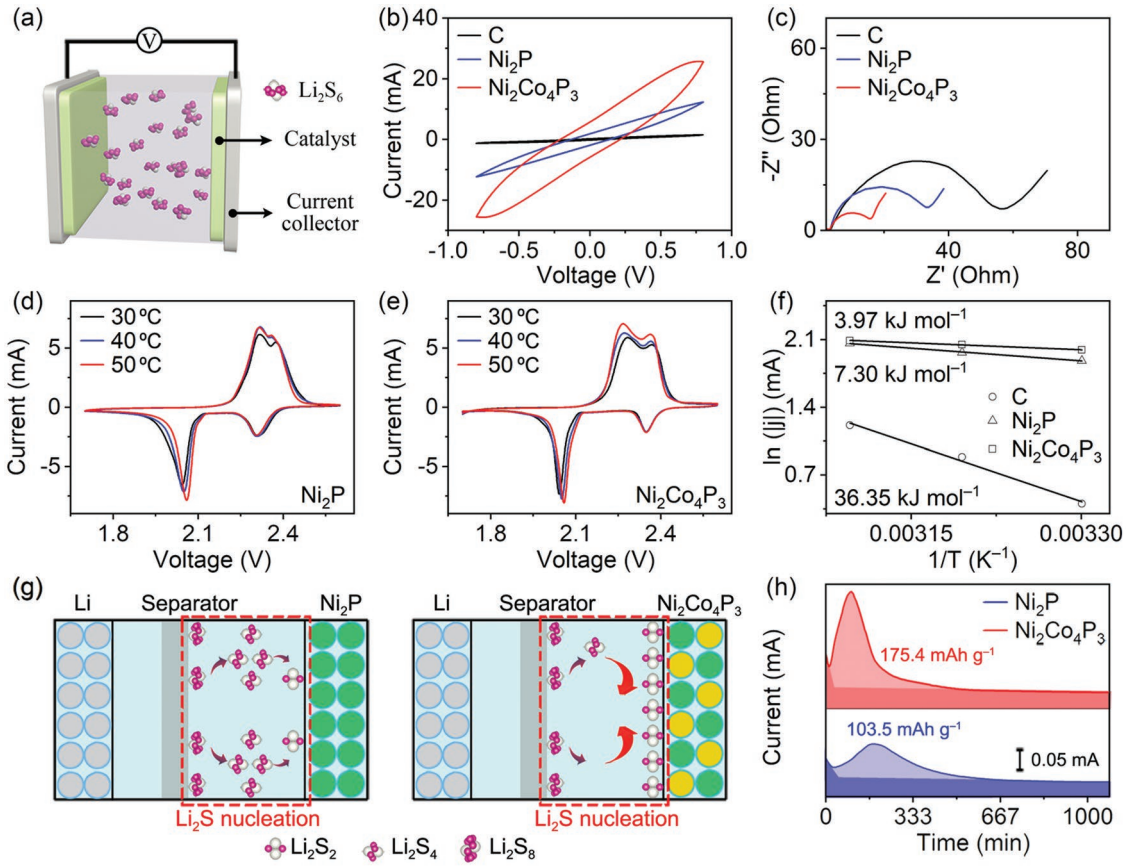


**Figure 2.** Electrochemical characterizations of Li–S kinetics: a) Schematic of a symmetric cell using two identical electrodes loaded with catalysts. b) CV curves and c) Nyquist plots of the symmetric cells with different catalysts. CV curves of the Li–S cells using d) $Ni_2P$ and e) $Ni_2Co_4P_3$ as catalysts at varied temperatures. f) Relation between CV peak current (≈2 V) and temperature for the C, $Ni_2P$, and $Ni_2Co_4P_3$ cells, respectively. g) Schematic illustration of $Li_2S$ nucleation tests using different catalysts. h) Chronoamperometry curves of $Li_2S_8$ solution discharged at 2.05 V on different catalysts (the light and dark colored regions indicate the precipitation of $Li_2S$ and the reduction of $Li_2S_8$/$Li_2S_6$, respectively).

show two voltage plateaus during discharge, which correspond to multistep lithiation of S species.[21–23] A symmetrical cell using two identical electrodes loaded with the same catalyst was constructed to study the conversion of $Li_2S_6$ (Figure 2a), which was dissolved in a mixed solvent of 1,2-dimethoxyethane (DME) and 1,3-dioxolane (DOL) as the electrolyte. Catalytic activities of $Ni_2P$ and $Ni_2Co_4P_3$ were measured using widely reported techniques like cyclic voltammetry (CV) and electrochemical impedance spectroscopy (EIS) methods. As Super P that is commonly used in S cathodes as the conductive agent may influence the discharge/charge process, we intentionally included the CV and EIS data of pure Super P for a clear comparison of catalytic activity. Figure 2b shows that $Ni_2Co_4P_3$ leads to higher CV currents than $Ni_2P$ whereas Super P induces nearly zero CV current, implying that $Ni_2P$ and $Ni_2Co_4P_3$ are catalytically active as compared to Super P.[24] A small diameter of the semicircle in the Nyquist plot of Figure 2c similarly indicates that the high catalytic capability of $Ni_2Co_4P_3$ significantly lowers the resistance of charge transfer, which will relatively suppress the polysulfide migration.[25]

The CV and EIS analyses show that $Ni_2Co_4P_3$ has high catalytic activity but do not reveal how active it is. These results or observation lacks the mechanistic or quantitative analysis of catalytic reactions. We further loaded catalysts into Li–S cells and conducted temperature-dependent CV measurements. Figure 2d,e shows that with the increase of temperatures, the CV peaks shift toward their corresponding equilibrium states, indicating the accelerated kinetics. More specifically, for the $Ni_2Co_4P_3$ cell, its reduction peak at ≈2 V has relative narrow shape and its oxidation peaks are clearly split. By comparing to the $Ni_2P$ cell, one can deduce that $Ni_2Co_4P_3$ promotes the conversion of polysulfides and accelerates their kinetics. The peak current is proportional to the reaction rates. After fitting the relation of peak currents and temperatures to the Arrhenius equation, the activation energy of polysulfide conversion is obtained by calculating the slope in Figure 2f (note that temperatures also affect the mobility of Li ions in electrolyte, which may more or less contributes to the calculated activation energy. However, the comparison is still valid under the same condition). Both $Ni_2P$ and $Ni_2Co_4P_3$ show much lower activation barriers than carbon. Especially, $Ni_2Co_4P_3$ has an ultralow barrier of only 3.97 kJ mol$^{-1}$, indicating rapid conversion kinetics, which further helps to increase the S utilization.

To verify the hypothesis, chronoamperometric nucleation experiments[26] were conducted using the test cells as illustrated in Figure 2g. These cells were galvanostatically discharged to

 

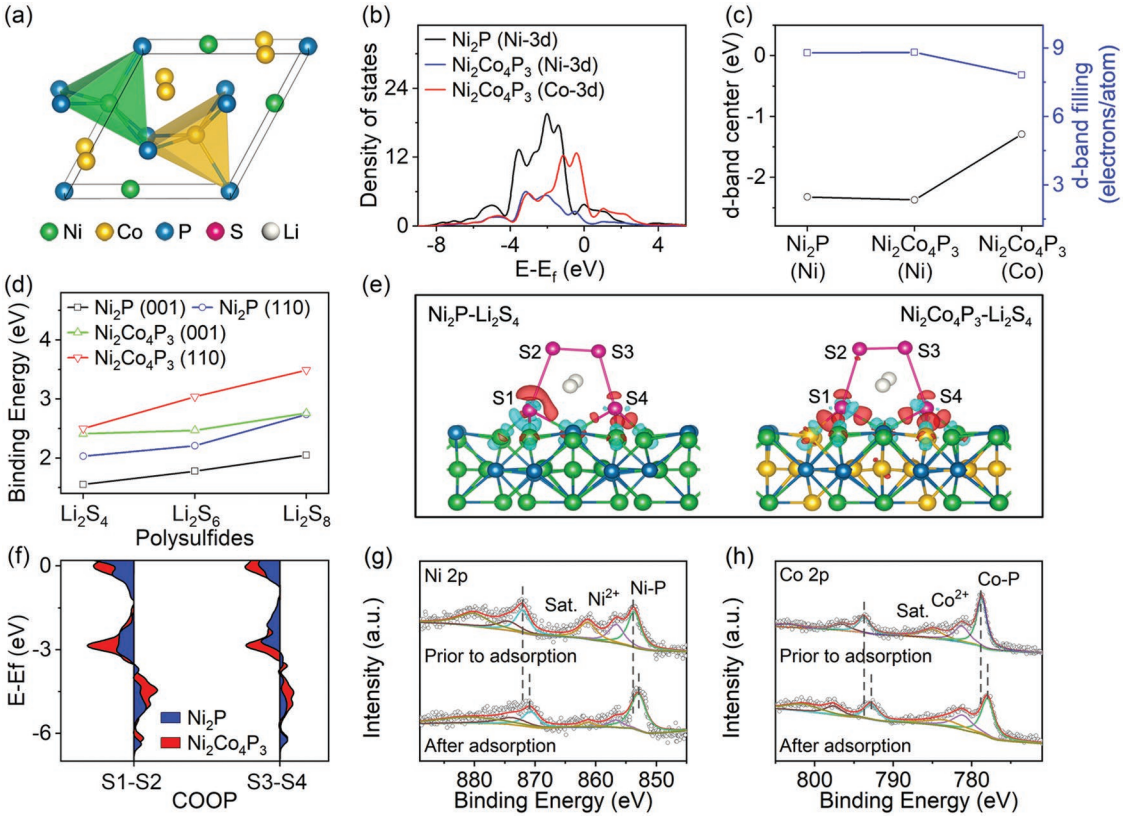


**Figure 3.** The interaction between polysulfides and different substrates via DFT calculations: a) Atomic structure model of hexagonal $Ni_2Co_4P_3$. b) PDOS and c) d-band electrons parameters for $Ni_2P$ and $Ni_2Co_4P_3$. d) Calculated binding strength for polysulfides and e) optimized adsorption configuration for $Li_2S_4$ on $Ni_2P$ slab and $Ni_2Co_4P_3$ slab. f) COOP diagram of the S1—S2 and S3—S4 bonds of $Li_2S_4$ adsorbed on $Ni_2P$ and $Ni_2Co_4P_3$. XPS spectra of g) Ni 2p and h) Co 2p of PNS-$Ni_2Co_4P_3$ prior to and after $Li_2S_4$ adsorption.

2.06 V at 50 mA $g^{-1}$ and then switched to a constant voltage protocol (2.05 V). Figure 2h presents the current response curves at 2.05 V. A sharp nucleation peak appears earlier in the $Ni_2Co_4P_3$ cell than in the $Ni_2P$ cell. More notably, the integrated area below the current curves is related to the nucleation capacity. A large capacity of 175.4 mAh $g^{-1}$ indicates that $Ni_2Co_4P_3$ can induce nucleation of more $Li_2S$ than $Ni_2P$ (103.5 mAh $g^{-1}$), which confirms the promotion of polysulfide conversion.[27] As far as the catalyst development for Li–S batteries is concerned, we can conclude that $Ni_2Co_4P_3$ exhibits a low activation barrier for the conversion reaction between $Li_2S_4$ and $Li_2S$ that is usually slow when catalysts are absent and thus, the utilization of S species is increased.

To decipher the activation process at molecular or atomic scales and rationalize the catalyst studies, we conducted a first principle calculation using the density functional theory (DFT). **Figure 3**a shows the geometric model of $Ni_2Co_4P_3$, which has a hexagonal structure with a $P\bar{6}2m$ space group.[28,29] $Ni_2Co_4P_3$ adopts a doped $Ni_2P$ structure with two third of Ni replaced by Co. Four possible geometric models exist for the stoichiometric composition of $Ni_2Co_4P_3$ (see Figure S3, Supporting Information). The crystallographic structure having the lowest formation energy was used for modeling. The states crossing the Fermi energy in Figure 3b indicate metallic properties, which reduce the resistance of charge transfer and electron conduction during battery cycling. A projected density of states (PDOS) analysis in Figure 3b shows that the Co 3d band in $Ni_2Co_4P_3$ is higher than the Ni 3d bands in $Ni_2Co_4P_3$ and $Ni_2P$. As the Co 3d band has a lower filling fraction and higher center than Ni 3d (Figure 3c), $Ni_2Co_4P_3$ may allow stronger interaction between metal sites and polysulfide molecules. The binding energy in Figure 3d confirms that polysulfide molecules are adsorbed more strongly on the surface of $Ni_2Co_4P_3$ than $Ni_2P$. Other adsorption configurations that include polysulfides on C, $Ni_2P$, and all four $Ni_2Co_4P_3$ structures were calculated as shown in Figures S4–S9 in the Supporting Information. A summary in Table S1 in the Supporting Information indicates that $Ni_2Co_4P_3$ has generally higher binding energy of polysulfides than C and $Ni_2P$.

To further understand how polysulfide molecules are activated during catalysis, we analyzed and discussed the $Li_2S_4$ adsorption on the (110) surface of $Ni_2P$ and $Ni_2Co_4P_3$ because $Li_2S_4$ has the highest binding energy on the most exposed (110) plane. Figure 3e displays that $Li_2S_4$ on $Ni_2Co_4P_3$ and $Ni_2P$ adopts a triply bridged adsorption configuration, whereby the terminal S atoms are bonded to three surface metal cations (see the top view in Figure S10, Supporting Information). By examining the bond length before and after adsorption in Table S2 in the Supporting Information, one can see that as compared to $Ni_2P$, $Ni_2Co_4P_3$ induces a short metal—S bond, confirming the high binding energy. The strong adsorption of polysulfides is helpful to relatively suppress their migration. More notably,

 

the S—S bond is more stretched on the surface $Ni_2Co_4P_3$ than $Ni_2P$, indicative of a weakened S—S bond. In addition, we analyzed the crystal orbital overlap population (COOP) of two terminal S—S bonds. Figure 3f indicates that the electron filling in the antibonding state of these two S—S bonds is higher for $Li_2S_4$ on $Ni_2Co_4P_3$ than that on $Ni_3P$. The energy cost to cleave the S—S bonds is reduced by the interaction between $Li_2S_4$ and $Ni_2Co_4P_3$, indicating that subsequent lithiation will overcome a low energy barrier.

To examine the calculation results on adsorption, we added $Ni_2Co_4P_3$ into an electrolyte containing $Li_2S_4$ for 1 h (Figure S11, Supporting Information). $Ni_2Co_4P_3$ can completely decolor the solution. By contrast, the electrolyte with carbon or $Ni_2P$ remains brown. It suggests that $Ni_2Co_4P_3$ strongly adsorbs $Li_2S_4$. Figure 3g shows the X-ray photoelectron spectroscopy (XPS) spectra of $Ni_2Co_4P_3$ prior to and after adsorbing $Li_2S_4$. The Ni 2p spectrum presents two main peaks of Ni $2p_{1/2}$ and $2p_{3/2}$ due to the spin–orbit splitting. After adsorbing $Li_2S_4$, the Ni 2p peaks of $Ni_2Co_4P_3$ shift to low binding energy, indicating the electron transfer from $Li_2S_4$ to Ni.[30] Similarly, the binding energy of Co 2p peaks is reduced more significantly as indicated by the vertical lines in Figure 3h, implying that polysulfides interact more strongly with Co than Ni sites of $Ni_2Co_4P_3$.[31] It should be noted that high binding energy facilitates the S—S bond breaking of $Li_2S_4$ and, however, it may retard the desorption of subsequent intermediates. To study the desorption process needs further theoretic calculation and analyses.

The above analyses confirm that $Ni_2Co_4P_3$ has a highly efficient catalytic activity for Li–S battery reactions and reveal that the interaction between polysulfides and $Ni_2Co_4P_3$ lowers the energy barrier of subsequent reactions. The methods that we used provide the base for rational catalyst developments. It is noted that polysulfides interact with the *d* bands of catalysts through the terminal S and the metal sites. When Co is doped into the $Ni_2P$ structure, the interaction relative to catalysis is strengthened because of the rise of Co 3d band. The maximum substitution ratio of $x$ in $Ni_xCo_{2-x}P$ is 0.2 (Ni:Co = 1:9), above which CoP appears (see Figure S12, Supporting Information, for details). CoP has a lower d-band center than $Ni_2Co_4P_3$, implying weak adsorption and catalytic activity (Figure S13, Supporting Information). Furthermore, we prepared five catalysts of $Ni_xCo_{2-x}P$ with varied Ni/Co ratios from 1:1 to 1:4 and tested their catalytic properties in symmetric cells. Figure S14 in the Supporting Information shows that $Ni_2Co_4P_3$ (Ni:Co = 1:2) has the largest current response among the five samples. Therefore, we focus on $Ni_2Co_4P_3$ to construct Li–S batteries in the following sections.

### 2.2. MLSC Construction

Efficient catalysts are essential to improve the performance of Li–S batteries. However, we also should emphasize that other strategies to suppress polysulfides migration are not less important and need to receive simultaneous and equal consideration in order to build better Li–S batteries. Therefore, we design an MLSC that hosts metallic $Ni_2Co_4P_3$ nanowires as the catalysts to maximize the effectiveness of catalysts. The fabrication procedure is illustrated in **Figure 4**a. A PNS is first constructed to form a 3D continuous network (Figure 4b) via a templated electrodeposition and selective etch according to our previous publications.[32–35] As PNS is derived from a template-etch route, the resultant channels are highly interconnected, facilitating ion transport during battery cycling. The metallic PNS serves as a rapid electron pathway and its large surface area is favorable to scaffold $Ni_2Co_4P_3$ nanowires (Figure 4c,d). During the preparation of MLSC, $Ni_2Co_4P_3$ nanowires were loaded onto PNS via the same method of hydrothermal synthesis and phosphorization as we made $Ni_2Co_4P_3$ nanowires powder for catalyst studies in Figure 2 (see the Figures S15 and S16, Supporting Information, for characterizations). The resultant composite structure (PNS-$Ni_2Co_4P_3$) has high-surface-area $Ni_2Co_4P_3$ nanowires rooted on a metallic conductive scaffold, which is ideal for an electrocatalytic process because the hierarchical structure is helpful to unfold the high catalytic activity of nanowires by maximizing electron conduction and charge transfer, thereby enhancing the kinetics of polysulfides conversion to a great extent.

It is worth noting that the nanowires are mesoporous (Figure 4e). The hollow interiors of $Ni_2Co_4P_3$ nanowires may result from the loss of water and carbon dioxide during annealing the precursor. When S is loaded onto the PNS-$Ni_2Co_4P_3$, we observed that the capillary effect due to the solvent ($CS_2$) evaporation leads to the distribution of S toward the roots of $Ni_2Co_4P_3$ nanowires as shown in Figure 4f,g. The EDX elemental mapping images in Figure 4h confirm that S is largely distributed close to the PNS surface and $Ni_2Co_4P_3$ roots. From a geometric perspective, it is understandable that the root region has a relatively large surface per unit volume, enabling a strong interaction between the $Ni_2Co_4P_3$ surface and S/polysulfides. Figure 4e shows the TEM image and EDX line scans of a S-loaded $Ni_2Co_4P_3$ nanowire. By comparing the elemental distributions across the diameter direction, one can see that S is also loaded into the porous structure of $Ni_2Co_4P_3$. Figure 4i further confirms the S distribution inside nanowires. S is an electronic insulator, which must be electrically wired for cycling. Due to the high conductivity,[36] $Ni_2Co_4P_3$ together with nickel scaffold provides the highly conducting pathway for electrochemical redox reactions.

At last, we developed an ion-selective filtration shell onto the monolithic electrode to block the polysulfide migration and only allow the Li-ion diffusion (see Figure S17, Supporting Information, and experimental for details). The shell consists of N-doped carbon microspheres (N-CMs) and sulfonated poly(ether ether ketone) (SPEEK). N-CMs have a strong affinity to polysulfides[37] whereas SPEEK is capable of exchanging Li-ions.[38] The SEM and EDX elemental mapping images in Figure 4j–m compare the cross-sections of two samples with and without the ion-selective filtration shell. The dark and thin layer in Figure 4l,m shows that the multifunctional filtration shell is embedded into the shallow channels of PNS-$Ni_2Co_4P_3$ to form a monolithic composite electrode. The EDX mapping image in Figure 4m indicates that carbon is only distributed on the top and bottom regions, where N-CMs and SPEEK sealed the open channels of PNS-$Ni_2Co_4P_3$. Such an MLSC design can accelerate the conversion reactions of S species with $Ni_2Co_4P_3$ and simultaneously separate polysulfides from Li-ion fluxes with the ion-selective filtration shell, forming a combined system of reaction and separation.

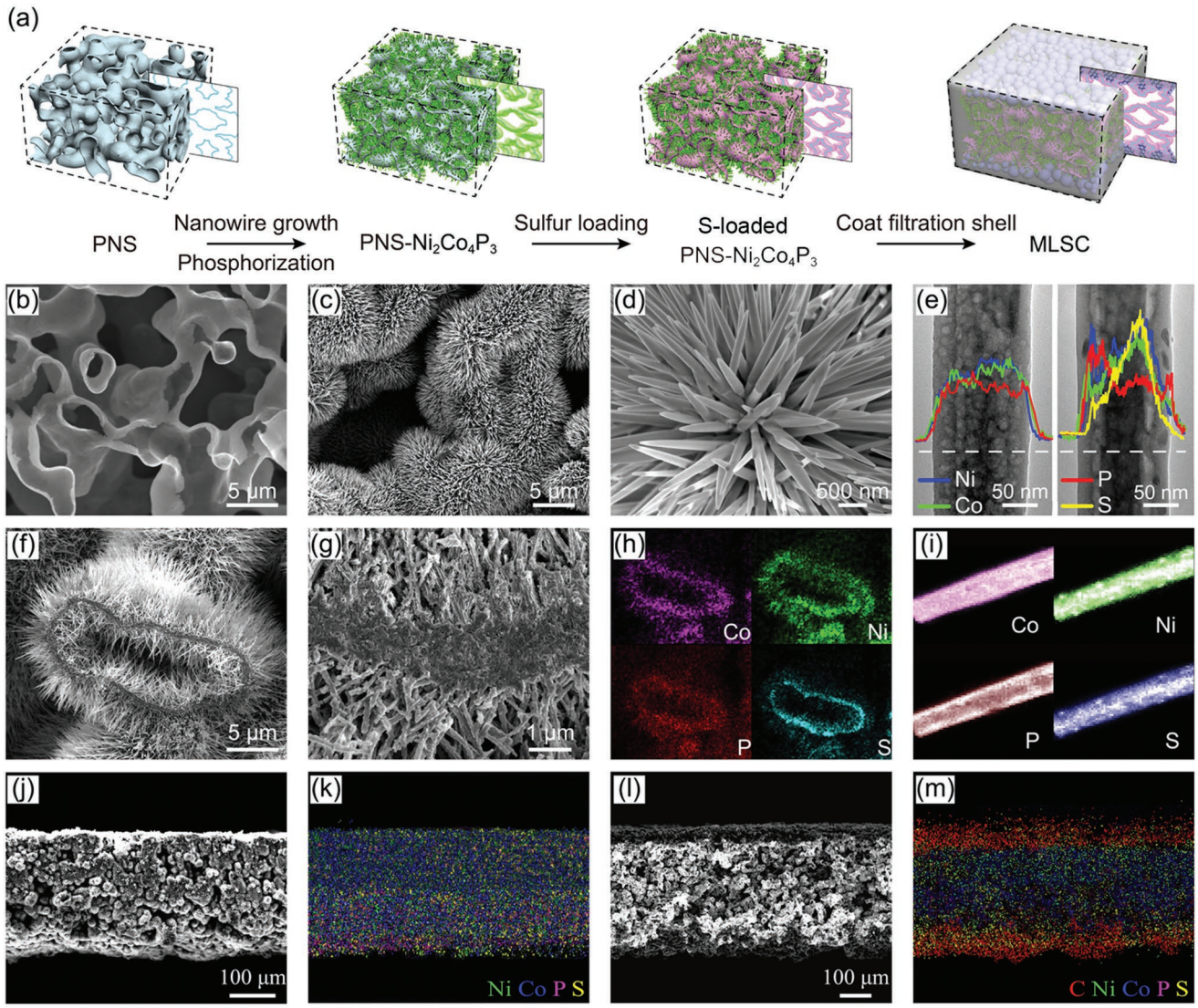


**Figure 4.** Schematic of fabrication process and characterizations of MLSC: a) Illustrated fabrication process. SEM images of b) PNS and c,d) PNS-$Ni_2Co_4P_3$. e) TEM and EDX plots of $Ni_2Co_4P_3$ nanowires before and after S loading. f,g) SEM and h) EDX elemental mapping images of S-loaded PNS-$Ni_2Co_4P_3$. i) EDX elemental mapping images of a S-loaded $Ni_2Co_4P_3$ nanowire. Cross-sectional j) SEM and k) EDX elemental mapping images of S-loaded PNS-$Ni_2Co_4P_3$. Cross-sectional l) SEM and m) EDX elemental mapping images of MLSC.

### 2.3. Electrochemical Properties of MLSC

The electrochemical properties of MLSCs were measured in coin cells with different S loading and compared to bare PNS and PNS-$Ni_2Co_4P_3$ without filtration layers (see Figures S18 and S19, Supporting Information, for the fabrication). **Figure 5**a shows that the CV curves at a scanning rate of 0.1 mV $s^{-1}$ of MLSC cells have two typical reduction peaks at 2.34 and 2.04 V. The reverse reactions manifest themselves with two oxidative peaks during charge.[39] Figure 5b presents the galvanostatic charge/discharge curves of MLSC at 0.1 C with the S loading of 5 mg $cm^{-2}$. A narrow gap of 0.16 V between charge and discharge indicates a low polarization. As shown in Figure 5c, the MLSC cell can deliver an initial capacity of 1223 mAh $g^{-1}$ at 0.1 C. After a minor decay, the MLSC cell maintains a relatively stable capacity of 1110 mAh $g^{-1}$ for next 100 cycles. The PNS-$Ni_2Co_4P_3$ cell shows a slow but continuous degradation of capacity. By comparing to the rapid decay of the PNS cell, one may infer that the $Ni_2Co_4P_3$ catalyst improves the cycling performance of the PNS-$Ni_2Co_4P_3$ cell because it accelerates the conversion of polysulfides and relatively suppresses polysulfide migration. The higher capacity retention of MLSC than PNS-$Ni_2Co_4P_3$ confirms that the multifunctional filtration shell works for blocking polysulfides. The cycling difference among the three cells further implies that the polysulfide issues of Li–S batteries must be addressed using multiple strategies and a single approach is usually unable to satisfactorily handle all related complexity.

The rate capability of the three samples is compared in Figure 5d. MLSC retains more capacity at high C rates than PNS and PNS-$Ni_2Co_4P_3$. A small semicircle diameter in the Nyquist plot (Figure 5e) confirms that MLSC has the lowest

 

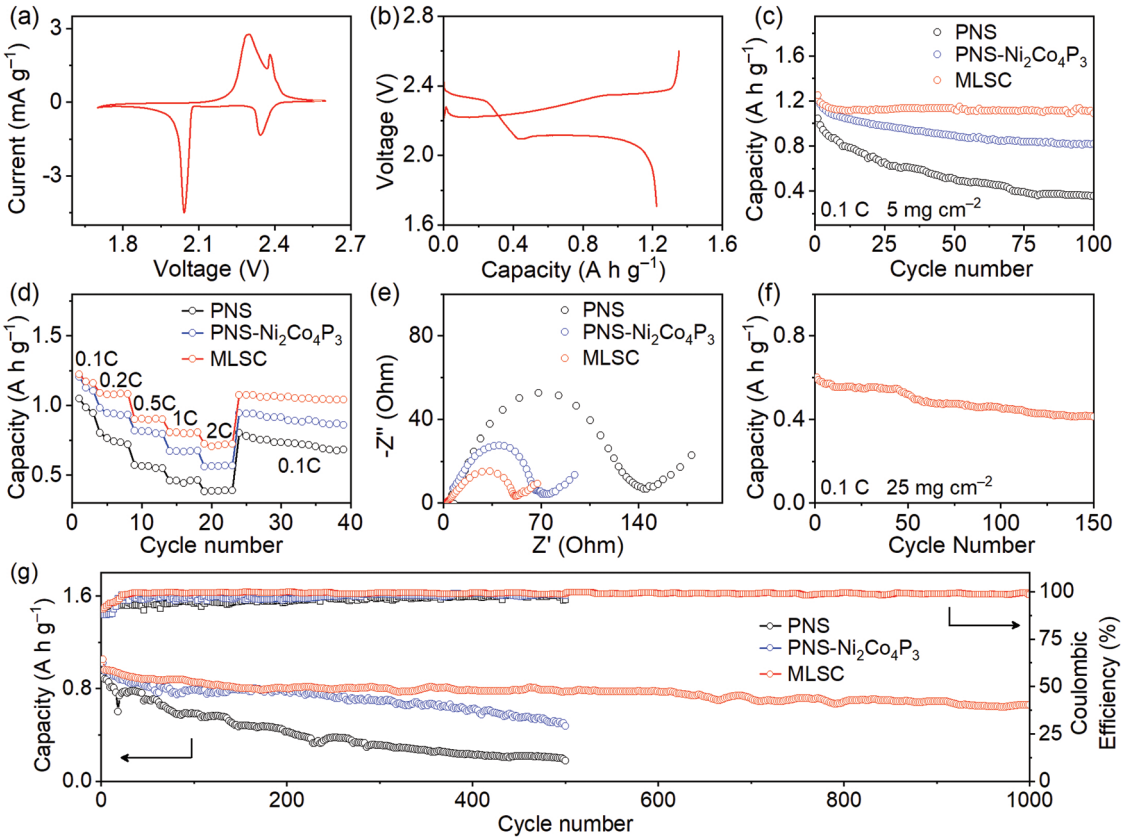


**Figure 5.** Electrochemical properties of MLSCs: a) CV curves and b) galvanostatic charge–discharge curves at 0.1 C. c) The capacity retention of the three electrodes at 0.1 C for 100 cycles. d) Rate properties, e) Nyquist plots of the cells using PNS, PNS-$Ni_2Co_4P_3$, and MLSC, respectively. f) Cycling properties at an ultrahigh S loading of 25 mg cm$^{-2}$. g) Long-term cycling stability of the three electrodes for 1000 cycles.

resistance of charge transfer, which is attributed to efficient catalysts, good electron pathways, and high surface area of MLSC.

The major advantage of MLSC is its capability of loading a large amount of S because it integrates reaction and separation into a microreactor-like cell to process S species-related conversion. Figure 5f presents the cycling performance of an MLSC cell with ultrahigh S loading of 25 mg cm$^{-2}$. At 0.1 C, it delivers an initial capacity of 602 mAh g$^{-1}$ (which corresponds to a gravimetric density of 567 Wh kg$^{-1}$ and volumetric density of 1003 Wh L$^{-1}$) and decreases with a rate of 1.26 mAh g$^{-1}$ per cycle. Until 150 cycles, it still retains 413 mAh g$^{-1}$ (10 mAh cm$^{-2}$). Such a good cyclability further corroborates the effectiveness of MLSC design, especially for high loading cells.

Long-term cycling was conducted for three samples with an S load of 5 mg cm$^{-2}$ at 1 C (Figure 5g). The PNS cell delivers an initial capacity of 899 mAh g$^{-1}$ and decays markedly to 176 mAh g$^{-1}$ in 500 cycles. By contrast, the PNS-$Ni_2Co_4P_3$ cell can maintain relatively high capacity upon cycling, indicating that the catalytic and adsorbing capability of $Ni_2Co_4P_3$ suppresses the polysulfide migration to some degree. The MLSC cell shows an initial capacity of 1051 mAh g$^{-1}$ with a CE of 90.8%. In the next 20 cycles, its CE rises to 99% and remains almost constant in the following cycles. The capacity slowly decreases upon cycling. Until 1000 cycles, the MLSC cell can still deliver a capacity of 658 mAh g$^{-1}$. In the first 20 cycles, the rapidly increasing CEs of the MLSC cell (as compared to PNS and PNS-$Ni_2Co_4P_3$) can be attributed to the multifunctional filtration shell. By comparing these cycling properties, one can see that the MLSC design can significantly improve the cycling stability of Li–S batteries because MLSC is able to regulate the reaction and separation processes.

### 2.4. Self-Discharge and Postmortem Analyses

To further study how effectively MLSC suppresses polysulfide migration, we assembled Li–S batteries in glass bottles for direct observation. As shown in **Figure 6**a, the electrolyte of the MLSC cell remains transparent up to 8 h whereas the electrolyte of the PNS cell turns yellow. There is a slight color change in the electrolyte of the PNS-$Ni_2Co_4P_3$ cell. It is believed that polysulfides diffuse out of the cathodes and color the electrolyte.[39–41] A transparent color implies that there is no significant amount of polysulfides in the electrolyte. We further conducted self-discharge tests on three cells (Figure 6b). Between two galvanostatic discharge/charge cycles, we applied a rest period of 24 h, which started at a plateau region (neither fully charged nor discharged) to allow soluble polysulfides to migrate. During the rest period, the open-circuit voltage (OCV) was monitored. A rapid voltage fade of PNS during OCV indicates severe self-discharge, which is mainly attributed to the polysulfide leakout.

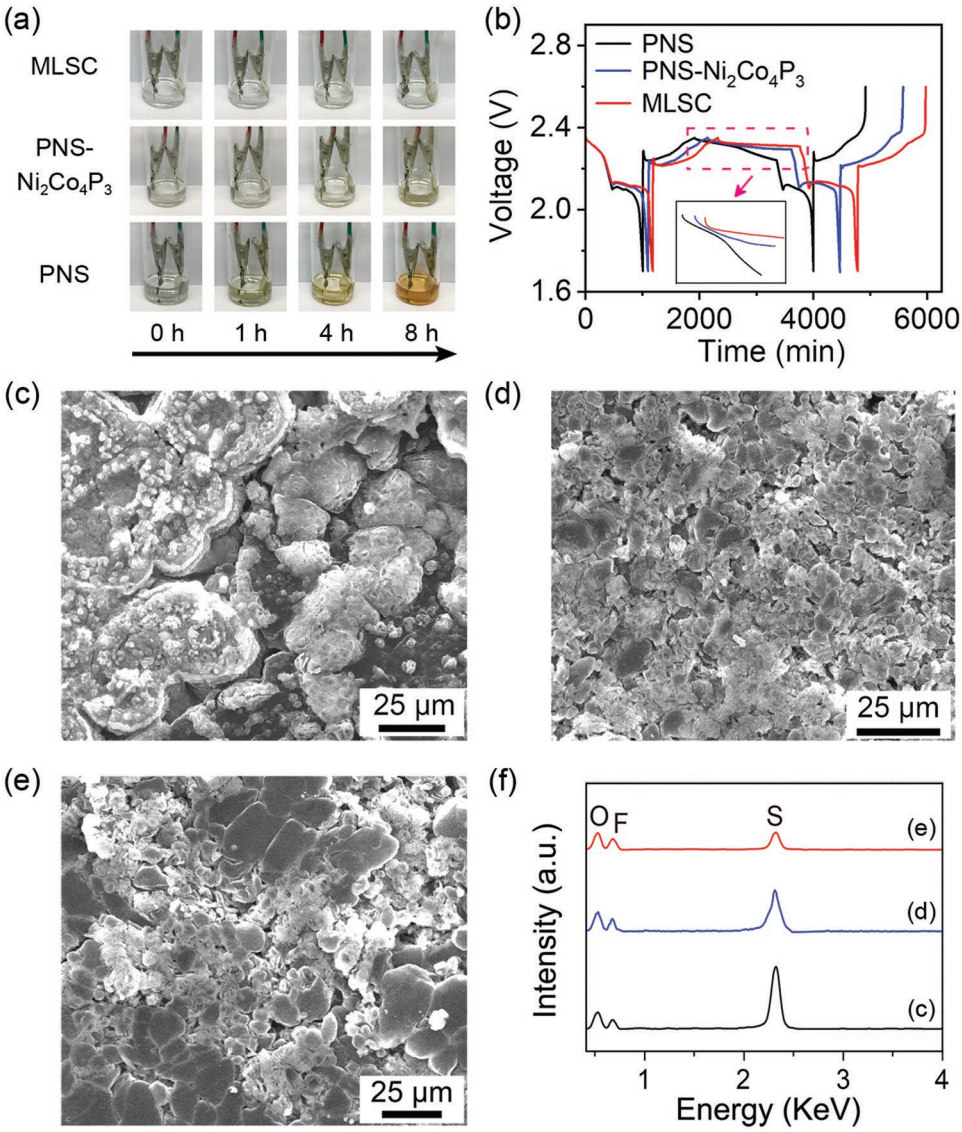


**Figure 6.** a) Optical images of the glass cells of PNS, PNS-$Ni_2Co_4P_3$, and MLSC during galvanostatic cycling. b) Voltage profiles of the PNS, PNS-$Ni_2Co_4P_3$, and MLSC cells during self-discharge tests (the inset is the zoomed-in voltage profiles during OCV). SEM images of the Li anodes of the cycled cells using the cathodes of c) PNS, d) PNS-$Ni_2Co_4P_3$, and e) MLSC. f) EDX plots of the cycled Li anodes.

For PNS-$Ni_2Co_4P_3$, a slight voltage drop indicates the much slower polysulfide migration, which is in agreement with the visualizing test in Figure 6a. In contrast, the MLSC cell demonstrates the most stable OCV profile among the three samples, implying the best suppression of self-discharge. The visualized cycling and self-discharge tests confirm that MLSC is able to confine the polysulfides inside the cathode and prevent the migration of polysulfides. It leads us to believe that the microreactor design appropriate addresses the polysulfide issues, yielding the high CEs and high capacity retention.

At last, the postmortem analysis was conducted to study the Li anodes that were disassembled from the cycled cells using PNS, PNS-$Ni_2Co_4P_3$, and MLSC. Figure 6c shows that the surface of the PNS-paired Li anode has been significantly changed to be rough and lumpy because polysulfides react with Li, leading to anodic corrosion.[42,43] The PNS-$Ni_2Co_4P_3$ cell shows a less rough surface on its Li anode (Figure 6d), indicating the minor corrosion. The MLSC-paired Li anode (Figure 6e) has relatively flat morphology, implying the inhibited polysulfide migration. The EDX scans in Figure 6f show that the PNS cell accumulates the largest amount of S on the Li surface. A plausible explanation is that the open channels of PNS are unable to properly prevent the polysulfide migration. The anode surface of the PNS-$Ni_2Co_4P_3$ cell shows much less S than that of the PNS cell because $Ni_2Co_4P_3$ nanowires array effectively adsorbs polysulfides. By contrast, the MLSC cell has the least amount of S species migrating to the Li anode because $Ni_2Co_4P_3$ adsorbs and catalyzes polysulfides and the filtration shell separates mobile polysulfides from Li-ion flux, blocking polysulfide diffusion toward Li anodes. In conjunction with the visualized cell and self-discharge tests, the postmortem characterizations confirm that the microreactor design suppresses the shuttle effects

of polysulfides, which significantly improves the cycling performance of Li–S batteries.

## 3. Conclusion

In summary, we prepared a novel $Ni_2Co_4P_3$ electrocatalyst for polysulfides conversion and revealed the molecular or atomic level picture of catalysis. Co dopants in the metal sites of $Ni_2P$ lift the d-band of $Ni_2Co_4P_3$, leading to a strong adsorption of polysulfides as compared to $Ni_2P$. As electrons transfer from polysulfides to $Ni_2Co_4P_3$, the activation energy to cleave the S—S bonds is lowered. Using the $Ni_2Co_4P_3$ catalyst, we further proposed a microreactor cathode strategy for ultrahigh S loading. The MLSC contains $Ni_2Co_4P_3$ nanowires catalysts, which are electrically wired by the 3D continuous PNS. An ion-selective filtration shell consisting of N-CMs and SPEEK seals the microreactor to limit polysulfides inside and allow Li-ions in and out of S cathodes. Thus, the shuttle effect is significantly reduced, leading to good long-term cyclability. MLSC can deliver an initial capacity of 1223 mAh $g^{-1}$ with a CE of 90.2%. The CE increase to 99.2% in ten cycles. At 1 C, the capacity only decreases from 1051 to 658 mAh $g^{-1}$ until 1000 cycles. Even at a high loading of 25 mg $cm^{-2}$, MLSC can still deliver a capacity of 413 mAh $g^{-1}$ (10 mAh $cm^{-2}$) for 150 cycles. The good catalytic activity and conductivity of $Ni_2Co_4P_3$ accelerate the polysulfides conversion and enhance the rate capability of MLSC cells. Generally, the microreactor design provides a new strategy to construct S cathodes with high performance and high loads.

## 4. Experimental Section

*Preparation of MLSC*: PNS was prepared according to our previous publications.[32–35] The resulting PNS was inserted into a solution of 0.004 M $Ni(NO_3)_2$, 0.008 M $Co(NO_3)_2$, and 0.012 M urea and transferred into a Teflon-lined stainless-steel autoclave at 100 °C for 8 h. The obtained sample was dried at 120 °C for 6 h and then annealed in a tube furnace with $NaH_2PO_2$ in the upstream of Ar gas at 300 °C for 2 h. $Ni_2Co_4P_3$ nanowires were grown onto the surface of PNS (denoted as PNS-$Ni_2Co_4P_3$). The PNS-$Ni_2Co_4P_3$ sample was soaked in a S-saturated $CS_2$ solution. After removing out of $CS_2$ solution, the sample was annealed at 155 °C for 4 h in Ar gas and S was loaded onto the $Ni_2Co_4P_3$ nanowire arrays of PNS to form a monolithic electrode of PNS-$Ni_2Co_4P_3$. The S loads could be increased by multiple rounds of soaking and annealing.

N-CMs were prepared by hydrothermal treatment of an aqueous solution containing 1 M glucose and 0.045 M ethylenediamine at 180 °C for 10 h.[37] The as-synthesized carbon microspheres were annealed at 600 °C in Ar gas. SPEEK was prepared according to previous reports.[38,44–47] About 0.15 g SPEEK and 1 g polyvinylidene fluoride (PVDF) were first dissolved in 10 mL *N*-methyl-2-pyrrolidone (NMP) and 0.2 g N-CMs were then dispersed into the mixture to form a slurry. The slurry was coated on the surface of PNS-$Ni_2Co_4P_3$ using a Doctor blade.

*Materials Characterizations*: XRD patterns were collected on a Rigaku D/MAX2500V with Cu $K_\alpha$ radiation ($\lambda$ = 1.5418 Å). SEM and EDX mapping images were obtained within a Zeiss Ultra 55 field-emission scanning electron microscope. High-resolution TEM (HRTEM) images were observed on an FEI Tecnai F20 microscope at 200 kV. XPS spectra were recorded on an ESCALab MKII X-ray photoelectron spectrometer with Mg K$\alpha$ X-ray as the excitation source. The binding energies in XPS analysis were corrected by referencing C 1s to 284.6 eV. The S load in the cathode was determined by a thermogravimetric analyzer (Figure S20, Supporting Information) (TGA, NETZSCH 209 F1 Libra) from room temperature to 900 °C in a nitrogen flow at a heating rate of 10 °C $min^{-1}$. The specific surface of PNS-$Ni_2Co_4P_3$ was measured to be 34.7 $m^2$ $g^{-1}$ by a Brunauer–Emmett–Teller method (kubo X1000, China, see Figure S21, Supporting Information).

*Polysulfide Adsorption Test*: 2 mg $mL^{-1}$ $Li_2S_4$ was synthesized by adding S and $Li_2S$ with a molar ratio of 3:1 in DME under vigorously stirring at 50 °C. An equivalent amount (50 mg) of C, $Ni_2P$, and $Ni_2Co_4P_3$ were added into 5 mL of the as-prepared $Li_2S_4$ solution, respectively. After 1 h, optical images were compared to show the difference in adsorption capability.

*Electrochemical Measurements*: All the samples were assembled with Li into 2032 coin cells in an Ar-filled glovebox. Celgard 2300 membrane was used as the separator. The electrolyte for Li–S cells was 1 M bis-(trifluoromethane) sulfonimide (LiTFSI) solution in 1:1 V:V mixture of DME and DOL with 1% $LiNO_3$. For 3D free-standing electrodes, the electrolyte in coin cells was controlled around 50 µL. Galvanostatic charge and discharge were conducted using a battery tester (Land, China). CV curves were measured on a potentiostat (Bio-Logic Science Instruments). EIS measurements were carried out between 100 kHz and 0.01 Hz.

*Kinetics Study*: Approximately 80 wt% catalysts ($Ni_2P$ or $Ni_2Co_4P_3$) were mixed with 10 wt% super-P and 10 wt% PVDF in NMP to form a slurry, which was then coated on Al foil. The loading of catalysts was ≈2 mg $cm^{-2}$. For symmetric cells, the electrolyte containing about 0.5 M $Li_2S_6$ and 1 M LiTFSI was prepared in DME and DOL (1:1, V:V) solution. The obtained catalysts electrodes were used as cathode and anode. CV measurements of these symmetric cells were conducted between –0.8 and 0.8 V at a scan rate of 50 mV $s^{-1}$. For $Li_2S$ nucleation tests, 0.3 M $Li_2S_8$ and 1 M LiTFSI in DME and DOL (1:1, V:V) solution was prepared. Li foil and Celgard 2300 membranes were used as the anode and separator. The as-prepared catalysts electrodes were used as cathodes. The cells were galvanostatically discharged at 50 mA $g^{-1}$ to 2.06 V and then maintained the voltage at 2.05 V to make $Li_2S$ nucleate and grow. The potentiostatic discharge was stopped after about 65 000 s.

*Temperature-Dependent Measurements*: Three typical S cathodes were prepared by mixing catalysts (C, $Ni_2P$, or $Ni_2Co_4P_3$), Super P, PVDF, and sulfur in NMP. The ratio of catalyst, super-P, and PVDF was 8:1:1 and the sulfur loading is 1.5 mg $cm^{-2}$. The resulting slurry was casted on the Al foil and dried at 60 °C overnight under vacuum. The S cathodes were assembled with Li metal foil into coin cells, which were then placed in a furnace. The temperatures were hold at 30, 40, and 50 °C, respectively. Two metallic wires were connected to Li–S batteries and led out to the potentiostat. CV curves were scanned at 0.1 mV $s^{-1}$. The setup is illustrated in Figure S22 in the Supporting Information.

## Supporting Information

Supporting Information is available from the Wiley Online Library or from the author.

## Acknowledgements

The authors acknowledge the financial support of the National Natural Science Foundation of China (21776121), Outstanding Youth Foundation of Jiangsu Province of China (BK20160012), National Key Research and Development Program of China (No. 2017YFA0205700), National Materials Genome Project (2016YFB0700600), "Jiangsu Shuanchuang" Program, and Thousand Youth Talents Plan. H.Z. thanks Jiangsu Donghai Silicon Industry Science and Technology Innovation Center. The numerical calculations in this paper have been done on the computing facilities in the High-Performance Computing Center (HPCC) of Nanjing University.

 

## Conflict of Interest

The authors declare no conflict of interest.

## Keywords

catalysis, lithium–sulfur batteries, microreactors, $Ni_2Co_4P_3$ nanowire arrays, polysulfide adsorption

Received: August 14, 2019
Revised: September 30, 2019
Published online: October 22, 2019

[1] J. Chang, J. Shang, Y. M. Sun, L. K. Ono, D. R. Wang, Z. J. Ma, Q. Y. Huang, D. D. Chen, G. Q. Liu, Y. Cui, Y. B. Qi, Z. J. Zheng, *Nat. Commun.* **2018**, *9*, 4480.
[2] Z. L. Xu, S. H. Lin, N. Onofrio, L. M. Zhou, F. Y. Shi, W. Lu, K. Kang, Q. Zhang, S. P. Lau, *Nat. Commun.* **2018**, *9*, 4164.
[3] W. L. Wu, J. Pu, J. Wang, Z. H. Shen, H. Y. Tang, Z. T. Deng, X. Y. Tao, F. Pan, H. G. Zhang, *Adv. Energy Mater.* **2018**, *8*, 1702373.
[4] L. Fan, M. Li, X. Li, W. Xiao, Z. Chen, J. Lu, *Joule* **2019**, *3*, 361.
[5] T. Li, X. Bai, U. Gulzar, Y. J. Bai, C. Capiglia, W. Deng, X. Zhou, Z. Liu, Z. Feng, R. Proietti Zaccaria, *Adv. Funct. Mater.* **2019**, *29*, 1901730.
[6] J. Pu, Z. Shen, J. Zheng, W. Wu, C. Zhu, Q. Zhou, H. Zhang, F. Pan, *Nano Energy* **2017**, *37*, 7.
[7] M. P. Yu, J. S. Ma, M. Xie, H. Q. Song, F. Y. Tian, S. S. Xu, Y. Zhou, B. Li, D. Wu, H. Qiu, R. M. Wang, *Adv. Energy Mater.* **2017**, *7*, 1602347.
[8] Z. H. Li, Q. He, X. Xu, Y. Zhao, X. W. Liu, C. Zhou, D. Ai, L. X. Xia, L. Q. Mai, *Adv. Mater.* **2018**, *30*, 1804089.
[9] Z. B. Cheng, Z. B. Xiao, H. Pan, S. Q. Wang, R. H. Wang, *Adv. Energy Mater.* **2018**, *8*, 1702337.
[10] Y. Wang, R. Zhang, J. Chen, H. Wu, S. Lu, K. Wang, H. Li, C. J. Harris, K. Xi, R. V. Kumar, S. Ding, *Adv. Energy Mater.* **2019**, *9*, 1900953.
[11] W. Kou, X. Li, Y. Liu, X. Zhang, S. Yang, X. Jiang, G. He, Y. Dai, W. Zheng, G. Yu, *ACS Nano* **2019**, *13*, 5900.
[12] B. Hao, H. Li, W. Lv, Y. Zhang, S. Niu, Q. Qi, S. Xiao, J. Li, F. Kang, Q.-H. Yang, *Nano Energy* **2019**, *60*, 305.
[13] Y. Zhong, D. L. Chao, S. J. Deng, J. Y. Zhan, R. Y. Fang, Y. Xia, Y. D. Wang, X. L. Wang, X. H. Xia, J. P. Tu, *Adv. Funct. Mater.* **2018**, *28*, 1706391.
[14] M. Zhao, H. J. Peng, Z. W. Zhang, B. Q. Li, X. Chen, J. Xie, X. Chen, J. Y. Wei, Q. Zhang, J. Q. Huang, *Angew. Chem., Int. Ed.* **2019**, *58*, 3779.
[15] Y. R. Zhong, K. R. Yang, W. Liu, P. He, V. Batista, H. L. Wang, *J. Phys. Chem. C* **2017**, *121*, 14222.
[16] Y. R. Zhong, L. C. Yin, P. He, W. Liu, Z. S. Wu, H. L. Wang, *J. Am. Chem. Soc.* **2018**, *140*, 1455.
[17] G. M. Zhou, H. Z. Tian, Y. Jin, X. Y. Tao, B. F. Liu, R. F. Zhang, Z. W. Seh, D. Zhuo, Y. Y. Liu, J. Sun, J. Zhao, C. X. Zu, D. S. Wu, Q. F. Zhang, Y. Cui, *Proc. Natl. Acad. Sci. USA* **2017**, *114*, 840.
[18] Z. Wang, J. Shen, J. Liu, X. Xu, Z. Liu, R. Hu, L. Yang, Y. Feng, J. Liu, Z. Shi, L. Ouyang, Y. Yu, M. Zhu, *Adv. Mater.* **2019**, *31*, 1902228.
[19] J. Zhou, X. Liu, L. Zhu, J. Zhou, Y. Guan, L. Chen, S. Niu, J. Cai, D. Sun, Y. Zhu, J. Du, G. Wang, Y. Qian, *Joule* **2018**, *2*, 2681.
[20] Y. Chen, W. Zhang, D. Zhou, H. Tian, D. Su, C. Wang, D. Stockdale, F. Kang, B. Li, G. Wang, *ACS Nano* **2019**, *13*, 4731.
[21] X. Yang, X. Gao, Q. Sun, S. P. Jand, Y. Yu, Y. Zhao, X. Li, K. Adair, L. Y. Kuo, J. Rohrer, J. Liang, X. Lin, M. N. Banis, Y. Hu, H. Zhang, X. Li, R. Li, H. Zhang, P. Kaghazchi, T. K. Sham, X. Sun, *Adv. Mater.* **2019**, *31*, 1901220.
[22] Z. W. Zhang, H. J. Peng, M. Zhao, J. Q. Huang, *Adv. Funct. Mater.* **2018**, *28*, 1707536.
[23] J. Conder, R. Bouchet, S. Trabesinger, C. Marino, L. Gubler, C. Villevieille, *Nat. Energy* **2017**, *2*, 17069.
[24] N. Wang, B. Chen, K. Qin, E. Liu, C. Shi, C. He, N. Zhao, *Nano Energy* **2019**, *60*, 332.
[25] Z. Xiao, Z. Yang, Z. Li, P. Li, R. Wang, *ACS Nano* **2019**, *13*, 3404.
[26] F. Y. Fan, W. C. Carter, Y. M. Chiang, *Adv. Mater.* **2015**, *27*, 5203.
[27] Y. Z. Song, W. Zhao, L. Kong, L. Zhang, X. Y. Zhu, Y. L. Shao, F. Ding, Q. Zhang, J. Y. Sun, Z. F. Liu, *Energy Environ. Sci.* **2018**, *11*, 2620.
[28] Q. Fu, T. Wu, G. Fu, T. Gao, J. Han, T. Yao, Y. Zhang, W. Zhong, X. Wang, B. Song, *ACS Energy Lett.* **2018**, *3*, 1744.
[29] S. Surendran, S. Shanmugapriya, A. Sivanantham, S. Shanmugam, R. Kalai Selvan, *Adv. Energy Mater.* **2018**, *8*, 1800555.
[30] J. R. He, Y. F. Chen, A. Manthiram, *Energy Environ. Sci.* **2018**, *11*, 2560.
[31] G. Li, X. L. Wang, M. H. Seo, M. Li, L. Ma, Y. F. Yuan, T. P. Wu, A. P. Yu, S. Wang, J. Lu, Z. W. Chen, *Nat. Commun.* **2018**, *9*, 705.
[32] J. Pu, Z. Liu, Z. Ma, J. Wang, L. Zhang, S. Chang, W. Wu, Z. Shen, H. Zhang, *J. Mater. Chem. A* **2016**, *4*, 17394.
[33] J. Li, J. Pu, Z. Liu, J. Wang, W. Wu, H. Zhang, H. Ma, *ACS Appl. Mater. Interfaces* **2017**, *9*, 25250.
[34] C. Zhu, Z. Liu, J. Wang, J. Pu, W. Wu, Q. Zhou, H. Zhang, *Small* **2017**, *13*, 1701260.
[35] Z. Liu, N. Feng, Z. Shen, F. Li, P. He, H. Zhang, H. Zhou, *ChemSusChem* **2017**, *10*, 2714.
[36] H. Liang, A. N. Gandi, D. H. Anjum, X. Wang, U. Schwingenschlogl, H. N. Alshareef, *Nano Lett.* **2016**, *16*, 7718.
[37] Z. Y. Wang, Y. F. Dong, H. J. Li, Z. B. Zhao, H. B. Wu, C. Hao, S. H. Liu, J. S. Qiu, X. W. Lou, *Nat. Commun.* **2014**, *5*, 5002.
[38] Y. D. Pan, Y. H. Zhou, Q. Zhao, Y. H. Dou, S. L. Chou, F. Y. Cheng, J. Chen, H. K. Liu, L. Jiang, S. X. Dou, *Nano Energy* **2017**, *33*, 205.
[39] Y. B. He, Z. Chang, S. C. Wu, Y. Qiao, S. Y. Bai, K. Z. Jiang, P. He, H. S. Zhou, *Adv. Energy Mater.* **2018**, *8*, 1802130.
[40] J. Q. Huang, Q. Zhang, H. J. Peng, X. Y. Liu, W. Z. Qian, F. Wei, *Energy Environ. Sci.* **2014**, *7*, 347.
[41] H. Q. Jiang, X. C. Liu, Y. S. Wu, Y. F. Shu, X. Gong, F. S. Ke, H. X. Deng, *Angew. Chem., Int. Ed.* **2018**, *57*, 3916.
[42] G. R. Li, W. Lei, D. Luo, Y. P. Deng, D. L. Wang, Z. W. Chen, *Adv. Energy Mater.* **2018**, *8*, 1702381.
[43] T. Lei, W. Chen, W. Lv, J. Huang, J. Zhu, J. Chu, C. Yan, C. Wu, Y. Yan, W. He, J. Xiong, Y. Li, C. Yan, J. B. Goodenough, X. Duan, *Joule* **2018**, *2*, 2091.
[44] M. Cheng, L. Li, Y. Chen, X. Guo, B. Zhong, *RSC Adv.* **2016**, *6*, 77937.
[45] Z. Li, Y. Han, J. Wei, W. Wang, T. Cao, S. Xu, Z. Xu, *ACS Appl. Mater. Interfaces* **2017**, *9*, 44776.
[46] K. Yang, L. Zhong, R. Guan, M. Xiao, D. Han, S. Wang, Y. Meng, *Appl. Surface Sci.* **2018**, *441*, 914.
[47] W. Lu, Z. Yuan, Y. Zhao, H. Zhang, H. Zhang, X. Li, *Chem. Soc. Rev.* **2017**, *46*, 2199.